

On-Policy Pixel-Level Grasping Across the Gap Between Simulation and Reality

Dexin Wang, Faliang Chang, Chunsheng Liu, *Member, IEEE*, Rurui Yang, Nanjun Li, and Hengqiang Huan

Abstract—Grasp detection in cluttered scenes is a very challenging task for robots. Generating synthetic grasping data is a popular way to train and test grasp methods, as is Dex-net and GraspNet; yet, these methods generate training grasps on 3D synthetic object models, but evaluate at images or point clouds with different distributions, which reduces performance on real scenes due to sparse grasp labels and covariate shift. To solve existing problems, we propose a novel on-policy grasp detection method, which can train and test on the same distribution with dense pixel-level grasp labels generated on RGB-D images. A Parallel-Depth Grasp Generation (PDG-Generation) method is proposed to generate a parallel depth image through a new imaging model of projecting points in parallel; then this method generates multiple candidate grasps for each pixel and obtains robust grasps through flatness detection, force-closure metric and collision detection. Then, a large comprehensive Pixel-Level Grasp Pose Dataset (PLGP-Dataset) is constructed and released; distinguished with previous datasets with off-policy data and sparse grasp samples, this dataset is the first pixel-level grasp dataset, with the on-policy distribution where grasps are generated based on depth images. Lastly, we build and test a series of pixel-level grasp detection networks with a data augmentation process for imbalance training, which learn grasp poses in a decoupled manner on the input RGB-D images. Extensive experiments show that our on-policy grasp method can largely overcome the gap between simulation and reality, and achieves the state-of-the-art performance. Code and data are provided at <https://github.com/liuchunsense/PLGP-Dataset>.

Index Terms—grasp detection, on-policy grasp, pixel-level grasp, parallel depth image

I. INTRODUCTION

Object grasping is a core issue in the field of robots [1][2]. Recently, many algorithms have claimed to be effective for handling stacked scenarios as well as grasping novel objects. There are currently two problems that are still unresolved, including on-policy grasping strategy and pixel-level exhaustive grasping generation.

(1) Some approaches train and test grasp policy on two different distributions [3–8], and this process belongs to off-policy grasping strategy. Parts of these methods calculate training grasps that are constrained to known 3D object surfaces while the learned policy predicts grasps from observations, such as Dex-Net [3–5] and GraspNet [6]. Pinto *et al.* [8] learn to grasp from 50K grasp tries and evaluate the grasp policy from RGB-D images. The data used to generate grasp labels is different from the test data, and the weak correlation between

Dexin Wang, Faliang Chang, Chunsheng Liu, Rurui Yang and Nanjun Li are with the School of Control Science and Engineering, Shandong University, Ji'nan, Shandong 250061, China (e-mail: flchang@sdu.edu.cn, liuchunsheng@sdu.edu.cn). (Corresponding author: Faliang Chang, Chunsheng Liu)

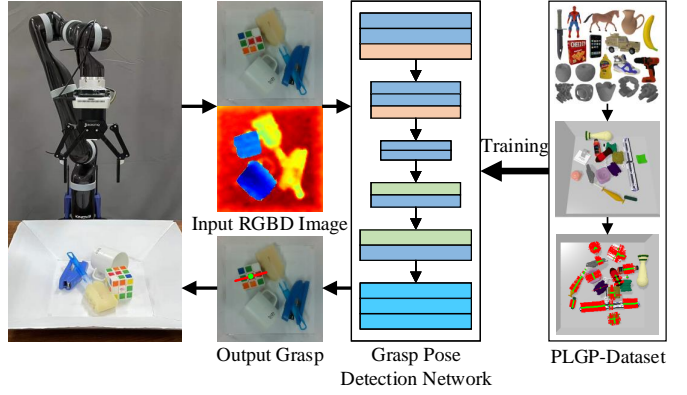


Fig. 1. Our on-policy grasping method. The grasp pose detection network is trained to generate grasp poses from RGB-D images using the PLGP-Dataset which consists of 45,550 synthetic RGB-D images and associated pixel-level grasp labels. Based on the output grasp with the maximal confidence, a robot is capable of successfully grasping objects.

data and labels prevents the algorithm from learning the correct mapping relationship, which may lead to reduced performance due to covariate shift [9].

(2) The training grasps of previous dataset are not exhaustive [3][10][11]. Dex-Net [3] generate grasp labels by sampling on the 3D object models due to large computation consuming of traversing the voxels. Cornell Dataset [10] is manually labelled with grasp rectangles, but human cannot accurately quantify abstract grasp and cope with cluttered scenes. Jacquard Dataset [11] collects sparse grasp labels by running random grasps in a simulated environment, which is time-consuming and cannot cover the full grasp space. Sparse labels cannot contain all positive samples and reduce sample variance, thereby reducing the generalization ability of the grasp policy.

For the first problem, we use depth images to compute grasp labels and validate grasp policy. Since the depth images based on the pinhole model cannot capture the information of occluded positions, previous methods cannot compute grasp poses based on depth images. We generate parallel depth images by projecting points in the scene parallel to the imaging plane, and compute robust grasps based on the images, and the learned policy detects grasps from observations. We refer to this as the *on-policy* method and distinguish this from prior methods that train and test on two different distribution.

For the second problem, we compute multiple robust grasp poses for each pixel in the image. Since computing the grasp centered on each voxel is extremely time-consuming, previous methods use sampling instead of traversal. We traverse the

pixels of the depth image to automatically generate dense pixel-level labels that covering the full grasp parameter space.

Based on the above solutions, we propose a Parallel-Depth Grasp Generation (PDG-Generation) method. The method first renders the camera depth image and parallel depth image for the stacked scene in the PyBullet simulation environment [12] based on the pinhole model and the parallel projection model, respectively. Then, multiple candidate grasp poses are generated for each pixel in the camera depth image. Finally, some checks based on parallel depth image are used to screen out robust grasp poses. Based on the automatic PDG-Generation, we build the first Pixel-Level Grasp Pose Dataset (PLGP-Dataset) that can serve as a base for training and evaluating grasp detection algorithms. PLGP-Dataset contains 45,550 RGB-D images taken from the different viewpoints of cluttered scenes. Each image is densely annotated, bringing over 58 million grasp poses.

We further construct a series of end-to-end network for learning grasp poses. To verify that our dataset can effectively improve the performance of existing networks, our networks are constructed based on five classical semantic segmentation networks and three grasp detection networks. A novel data augmentation method is proposed to increase positive samples to reduce the impact of data imbalance on network training. Meanwhile, we contribute a simulation bin-picking benchmark that can provide synthetic RGB-D images and point clouds embedded with noise, and drive the simulated robotic arm to grasp object according to a given grasp pose.

The proposed on-policy method is shown in Fig. 1. We compare our method with previous methods in the benchmark, and conduct robotic experiments in real-world. Experiments demonstrate that our method can overcome the gap between simulation and reality, and achieves the state-of-the-art performance.

The contributions of our study are summarized as follows:

- 1) We propose an on-policy grasp method that avoid covariate shift caused by training and testing the network on different distributions.
- 2) We propose a Parallel-Depth Grasp Generation (PDG-Generation) method to collect RGB-D images and generate pixel-level grasp labels.
- 3) The first Pixel-Level Grasp Pose Dataset (PLGP-Dataset) is built which can serve as a base for training and evaluating grasp pose detection algorithms.
- 4) Based on the PLGP-Dataset, we train a series of grasp detection networks which achieve the state-of-the-art performance.

II. RELATED WORK

The goal of grasp detection is to output a gripper pose using the visual information of cluttered scenarios, and the gripper can stably grasp the target when closing the jaws in this posture. The methods can be roughly divided into analytic methods and empirical methods [17]. Analytic methods first use the object model to generate stable grasps, and then obtain the reachable grasp according to the object pose in the scene. Yet, they are usually not applicable to objects

whose models are unknown. In contrast, empirical methods do not require object 3D models; they train the grasp model using known objects and use the model to detect the grasp posture of unknown objects [18][19][20]. In recent years, deep learning based methods have attracted the attention of many researchers.

Dataset. In order to train the grasp detection network, many datasets are proposed. Cornell dataset [10] collects RGB-D images of scenes containing a single object, and manually annotates rectangle grasp pose. [13][8] use real robots for random grasping, and records the successful grasps pose as labels. These dataset generation methods are time-consuming and insufficient to cover all the grasp parameter space. To avoid such problem, [11] uses 3D object models to build cluttered scenes in simulation environment, and uses simulation robots to collect grasp labels. The simulation-based method improves efficiency, but the grasp labels are still sparse. Mahler *et al.* first calculate 6-DOF grasps on the 3D object models through force-closure metric [21], then obtains the 4-DOF grasp pose perpendicular to the table [5][4]. To avoid the gap from simulation to reality, Fang *et al.* construct 3D models of real objects to sample 6-DOF grasp poses, and record point clouds of real stacked scenes to train grasp detection networks [6]. However, networks trained on these datasets need to fit functional relationships from images or point clouds to grasp poses generated based on 3D models, and the difference in data distribution reduces the performance of networks. On the contrary, we propose a label generation method that works directly on depth images and avoids differences in the data distribution of training network.

Network. Based on different grasp pose representations, grasp detection networks are mainly divided into three categories: grasp quality classification networks, 4-DOF networks based on RGB-D images, and 6-DOF networks based on point clouds. Based on grasp quality classification networks, Dex-Net [3–5] first samples multiple candidate grasp poses on the depth image, and then uses the network to evaluate the quality of each grasp. This method is less efficient and the candidate grasps cannot cover the grasp parameter space. Based on 4-DOF networks, discrete or pixel-level 4-DOF grasp poses are predicted end-to-end [22–26]. Fewer degrees of freedom limit the reach of the gripper. Based on 6-DOF networks, sparse 6-DOF grasp poses are predicted in a decoupled manner [6][27–31]. However, the extreme imbalance of positive and negative samples makes the 6-DOF networks difficult to train. In this work, we validate that the 4-DOF network trained on our new dataset performs better than previous 6-DOF networks.

III. PARALLEL-DEPTH GRASP GENERATION METHOD

A. Overview

As far as the literature we can find, most previous grasp datasets are manually annotated or automatically annotated based on sampling. Due to the deviation between human subjectivity and actual grasping, the manually labeled grasp poses are sparse and inaccurate [10]. GraspNet [6] and Dex-Net [4] first sample grasp poses based on 3D object, and then screen out the grasp labels that do not collide with scene.

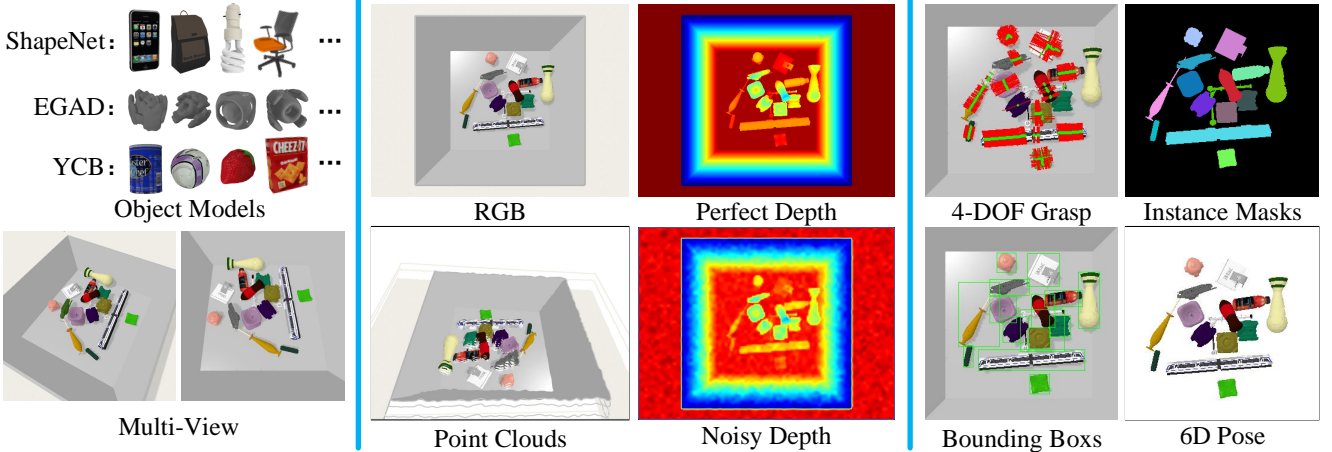


Fig. 2. The key components of PLGP-Dataset. RGB-D images are rendered in pybullet simulation environment from different views. The grasp poses, the 6D pose of each object, the bounding boxes and the instance masks are annotated.

TABLE I
SUMMARY OF THE PROPERTIES OF PUBLICLY AVAILABLE GRASP DATASETS.

Dataset	Grasps per image	Objects per image	Grasp label	Modality	Total objects	Total grasps	Total images	Data source	Automatized generation	Pixel level	On-policy
Cornell [10]	~8	1	Rect.	RGB-D	240	8,019	1,035	Cam.	No	No	No
Pinto <i>et al.</i> [8]	1	-	Rect.	RGB-D	150	50K	50K	Cam.	Yes	No	No
Levine <i>et al.</i> [13]	1	-	Rect.	RGB-D	-	800K	800K	Cam.	Yes	No	No
Dex-Net 2.0 [4]	1	1	4-DOF	Depth	1,500	6.7M	6.7M	Sim.	Yes	No	No
Dex-Net 2.1 [5]	1	~5	4-DOF	Depth	1,500	102.6K	102.6K	Sim.	Yes	No	No
Jacquard [11]	~20	1	Rect.	RGB-D	11k	1.1M	54K	Sim.	Yes	No	No
VMRD [14]	~20	~3	Rect.	RGB	-	100K	4,683	Cam.	No	No	No
Multi-Object [15]	~30	~4	Rect.	RGB-D	-	2904	96	Cam.	No	No	No
VR-Grasping-101 [16]	100	1	6-DOF	RGB-D	101	4.8M	10K	Sim.	Yes	No	No
GraspNet-1Billion [6]	3~9M	~10	6-DOF	RGB-D	88	1.2B	97K	Cam.	Half	No	No
PLGP-Dataset (Ours)	~1280	5/15	4-DOF	RGB-D	4,555	58M	45,550	Sim.	Yes	Yes	Yes

Rect.: Grasp rectangle [10]. Cam.: Camera. Sim.: Simulation.

However, sparse sampling cannot cover the full grasp space, which reduces the generalization of the network. To overcome these problems, we generate accurate and pixel-level grasp labels by traversing the pixels of the depth image.

Compared to previous dataset generation methods, our Parallel-Depth Grasp Generation (PDG-Generation) method has three advantages: (1) Grasp labels are generated at the pixel level. We iterate over all pixels to compute grasps to avoid missing ground-truth. (2) The method is on-policy which enables grasp networks to train and test on the same distribution, while traditional methods train and test on different distributions. (3) The dataset construction process is automatic, so it can be easily and unlimitedly expanded.

Based on the PDG-Generation, we construct a dataset in cluttered scenario for pixel-level grasp pose detection named on PLGP-Dataset. The dataset contains 9,110 simulated cluttered scenes, and each contributes five RGB-D images from different views, bringing 45,550 images in total. We also provide noise-added depth images to simulate real camera. The grasp poses for each image varies from 100 to 7,000,

and in total our dataset contains over 58 million grasp poses. Besides, we also provide accurate object 6D pose annotations, object masks and bounding boxes. Fig. 2 illustrates the key components of our dataset. A summary of the properties of public grasp datasets can be found in Table I.

B. Data Collection

Our dataset contains 4,555 3D object models from three model datasets including: 2,204 synthetic models from ShapeNet [32], 70 laser scans from the YCB object database [33], and 2,281 synthetic models from EGAD [34]. All objects are diverse in shape and size, and scaled to fit the gripper. To collect data of cluttered scene, a simulated camera with a vertical field of view of 60 degrees and output image size of 480×640 is constructed. The camera intrinsic matrix is calculated as follows:

$$M = \begin{bmatrix} \frac{240}{\tan(fov/2)} & 0 & 319.5 \\ 0 & \frac{240}{\tan(fov/2)} & 239.5 \\ 0 & 0 & 1 \end{bmatrix} \quad (1)$$

where fov is the vertical field of view.

Two sets of stacked scenes containing 5 and 15 random objects, respectively, are constructed. The objects are loaded into the simulation environment in random poses and fall freely into the tray to form cluttered scenes. For each scene, we collect 5 pairs of synchronized RGB-D images and corresponding camera poses from different viewpoints. Each camera pose T is calculated by initial pose T_i and offset pose T_o :

$$T = T_i \cdot T_o \quad (2)$$

where T_i denotes the pose that the camera is above the scene and the z-axis of camera is facing and perpendicular to the center of the tray. The translation vector t_o and euler angles R_o of T_o are defined by formula (3) and formula (4), respectively:

$$t_o = [2l\alpha_1 - l, 2l\alpha_2 - l, 0]^T \quad (3)$$

$$R_o = [-\tan(\frac{t_0[0]}{z}), \tan(\frac{t_0[1]}{z}), 0]^T \quad (4)$$

where l defines the maximum translation of the camera in the x-y plane, α_1 and α_2 are random numbers in the range [0,1] and specify the scale of camera translation along the x and y axes, respectively. z is the height of the camera from the tray when it is in the T_i pose. The pose T keeps the camera z-axis pointing at the center of the tray, so that all objects are included in the rendered image. The mask and pose of objects are exported by pybullet [12].

To stick as close as possible to real depth images, instead of only adding Gaussian noise to the perfect depth image as in [35], we follow the steps below to generate a more realistic depth image:

- (1) The values in the image are probabilistically set to 0, and the probability is calculated from the local gradient of the point. The processed image is:

$$I_1 = \begin{cases} 0 & \delta < f(\text{grad}) \\ I & \text{otherwise} \end{cases} \quad (5)$$

where I denotes the perfect depth image, δ is a random number from 0 to 1, and $f(\text{grad})$ is a linear function that scales the gradients to the range [0,1]. Points with large gradients have a high probability of being zeroed. The purpose is to simulate the missing regions of the depth image where the depth varies greatly.

- (2) Gaussian noise is added to the image I_1 to simulate the depth error of real cameras. The processed image is $I_2 = I_1 + \epsilon$ where ϵ is zero-mean Gaussian noise over pixel coordinates.
- (3) The image I_2 is sequentially scaled down by n times and upscaled to original size. The purpose is to remove small depth variations, which are often not captured by real RGB-D camera.

C. Grasp Definition

A 6-DOF grasp pose of parallel-jaw gripper is defined as:

$$g = [t, R, w] \quad (6)$$

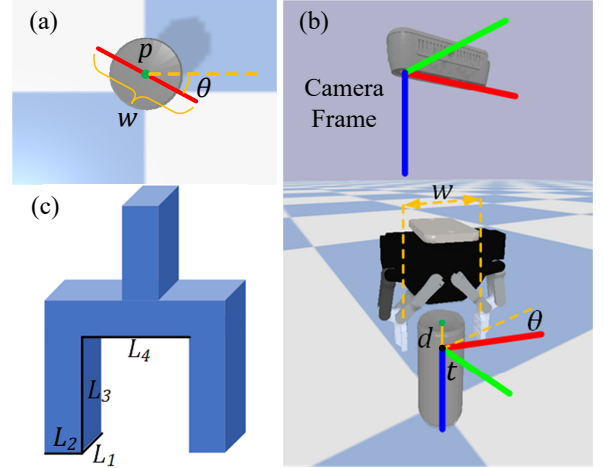


Fig. 3. (a) A 4-DOF grasp pose is defined by grasp point p , gripper approaching distance d , rotation around the camera z-axis θ and gripper width w . (b) The 6-DOF grasp pose calculated based on 4-DOF grasp pose. (c) Gripper size is denoted by $[L_1, L_2, L_3, L_4]$.

where $t \in \mathbb{R}^{3 \times 1}$ denotes the center of the gripper, $R \in \mathbb{R}^{3 \times 3}$ denotes the gripper orientation and $w \in \mathbb{R}$ denotes the gripper opening width. For neural network that take images as input, directly learning the translation vector in $\mathbb{R}^{3 \times 1}$ and rotation matrix in $\mathbb{R}^{3 \times 3}$ is not intuitive [6]. Instead, we simplify the grasp pose g to a 4-DOF grasp \tilde{g} parallel to the camera's z-axis:

$$\tilde{g} = [p, d, \theta, w] \quad (7)$$

where $p \in \mathbb{R}^{2 \times 1}$ is the grasp point in the image, $d \in \mathbb{R}$ denotes the gripper approaching distance at p , and $\theta \in \mathbb{R}$ denotes the angle between the gripper closing direction and the image horizontal axis. The grasp pose g in camera coordinate system is calculated given \tilde{g} and camera intrinsic matrix M :

$$t = \frac{M^{-1}}{I(p)} \begin{bmatrix} p \\ 1 \\ 1 \end{bmatrix} + \begin{bmatrix} 0 \\ 0 \\ d \end{bmatrix} \quad (8)$$

$$R = \begin{bmatrix} \cos\theta & \sin\theta & 0 \\ -\sin\theta & \cos\theta & 0 \\ 0 & 0 & 1 \end{bmatrix} \quad (9)$$

where $I(p)$ denotes the value of the depth image I at grasp point p . Fig. 3 explains our formulation of grasp pose.

D. Parallel Depth Image based Grasp Annotation

Most previous grasp datasets have sparse labels, and different distributions for test and training, which reduces the performance. Since depth images are widely used for grasp detection, we compute dense grasp labels based on depth images. The usual depth image is generated based on TOF or structured light [36] which are actually pinhole imaging models, so some information in the scene cannot be collected due to occlusion (Fig. 5 (a)). To solve the above problems, we propose a Parallel-Depth Grasp Generation (PDG-Generation) method. The method first generates a parallel depth image

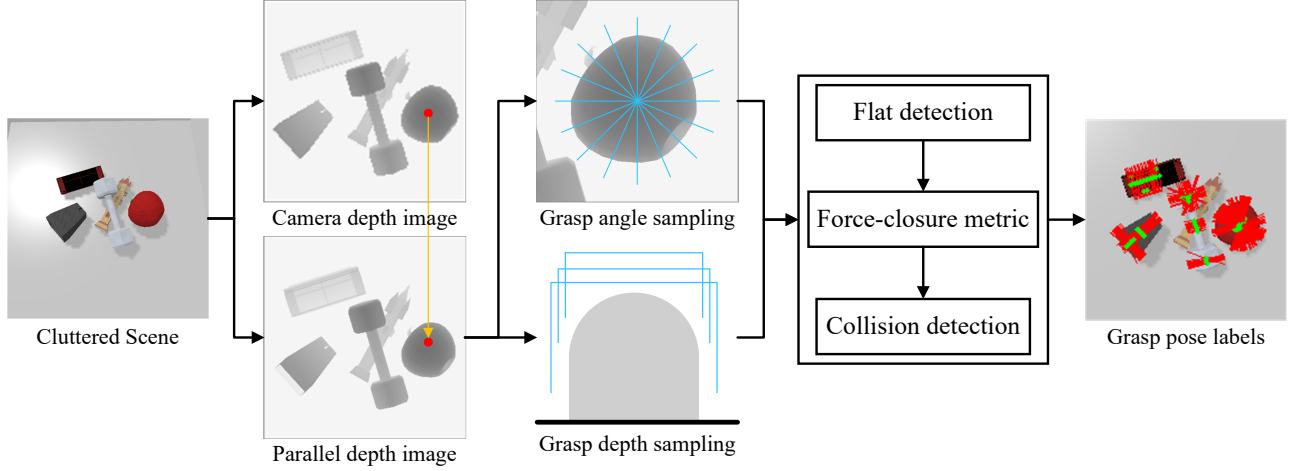


Fig. 4. Grasp pose annotation pipeline. The camera depth image and parallel depth image are firstly rendered. Then the grasp angle and grasp depth are sampled for every point in camera depth image. The grasp width is calculated based on collision detection. Finally, a series of checks are performed to avoid invalid grasps. In the grasp pose labels, each green point represents grasp point p , and the direction and width of the red line centered on the green point represent the grasp angle θ and grasp width w , respectively.

of the scene, then aligns the pixels in the image with the points in the camera depth image, and finally computes robust grasp poses using the parallel depth image. The automated annotation pipeline is illustrated in Fig. 4, and the detailed process is described as follows.

For the convenience of description, let I_c and I_p denote the usual camera depth image and our parallel depth image, respectively, let O , X and C denote the coordinate system of the 3D object model, the simulation environment and the simulated camera respectively.

1) *Parallel depth image generation*: Different from the camera depth image I_c , projection lines of points in the scene that generate parallel depth image are parallel to each other instead of meeting at the optical center, which is illustrated in Fig. 5. In our experiments, the imaging plane of the image I_p coincides with the x - y plane of the camera coordinate system C , so the image I_p can be generated using the parameters of the simulated camera.

For a point p_O on the 3D object surface, the projected point $p_C = [x_C, y_C, z_C]$ in the camera coordinate system C is formulated as:

$$p_C = T_C^X \cdot T_X^O \cdot p_O \quad (10)$$

where $T_C^X \in \mathbb{R}^{4 \times 4}$ denotes the transformation matrix of coordinate system X relative to C , and $T_X^O \in \mathbb{R}^{4 \times 4}$ denotes the transformation matrix of coordinate system O relative to X . Then, the projected point $\tilde{p} = [\tilde{c}, \tilde{r}]^T$ of p_C in the image I_p of size $H \times W$ is formulated as:

$$\begin{bmatrix} \tilde{c} \\ \tilde{r} \\ 1 \end{bmatrix} = \begin{bmatrix} \eta & 0 & (W-1)/2 \\ 0 & \eta & (H-1)/2 \\ 0 & 0 & 1 \end{bmatrix} \cdot \begin{bmatrix} x_C \\ y_C \\ 1 \end{bmatrix} \quad (11)$$

where \tilde{c} and \tilde{r} respectively represent the column and row coordinates of \tilde{p} with the upper left corner of the image I_p as the origin. η is the projection ratio of the actual length in the image (5,000 in this study). The depth value of the image

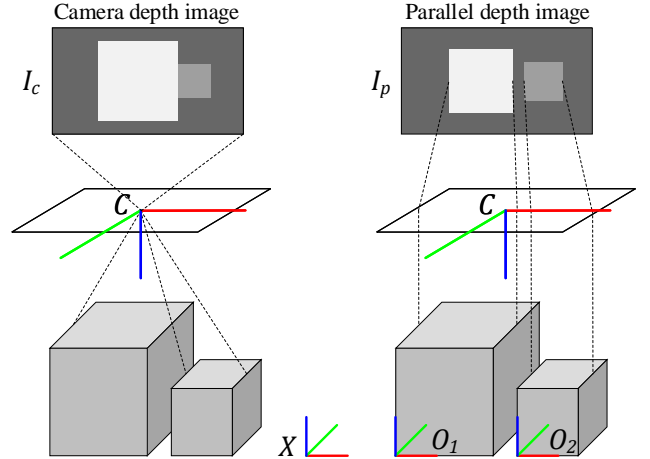


Fig. 5. The illustration of camera depth image I_c and parallel depth image I_p . I_c is generated based on the pinhole imaging models. I_p is generated by scaling the x and y coordinates of point in the camera coordinate system C . The gap between two objects is lost in image I_c , and preserved in image I_p . The coordinate system of the scene consists of the simulated environment X , objects O and camera C .

I_p at coordinate \tilde{p} is z_C . Fig. 5 shows the simplified principle of generating camera depth image and parallel depth image, the gap between two objects is lost in image I_c , and preserved in image I_p .

2) *Pixel alignment*: In order to calculate the pixel-level grasp pose, we traverse each pixel on I_c and calculate the aligned point on the image I_p , and use the aligned point as the grasp center to calculate the robust grasp pose.

For a point p in the object mask in the camera depth image I_c , the projected point p_C in the camera coordinate system C is formulated as:

$$p_C = \frac{M^{-1}}{I_c(p)} \begin{bmatrix} p \\ 1 \end{bmatrix} \quad (12)$$

Then, the aligned point $\tilde{p} = [\tilde{c}, \tilde{r}]^T$ in the image I_p is

calculated by:

$$\begin{bmatrix} \tilde{p} \\ 1 \end{bmatrix} = \begin{bmatrix} \eta & 0 & (W-1)/2 \\ 0 & \eta & (H-1)/2 \\ 0 & 0 & 1 \end{bmatrix} \cdot \begin{bmatrix} x_C \\ y_C \\ 1 \end{bmatrix} \quad (13)$$

3) *Grasp pose calculation*: We use the point \tilde{p} as the grasp center to calculate the robust grasp pose on the image I_p . For the point \tilde{p} , grasp angle θ and grasp depth d are searched in a two dimensional grid $\Theta \times D$, where $\Theta = \{\frac{k \cdot \pi}{K} | 0 \leq k < K, k \in N\}$ and $D = \{k \cdot g | 0 \leq k \cdot g < L_3, k \in N\}$. K is the number of grasp angle samples, we experimentally set $K = 18$. g is the grasp depth sampling interval, we set $g = 0.002m$. L_3 represents the maximum grasp depth of the gripper. Gripper width w is set to the opening width when the gripper just collides with the object plus tolerance ($0.005m$ in our experiments). In order to facilitate the calculation of the physical collision between the gripper and object, gripper size is denoted by $[L_1, L_2, L_3, L_4]$, as shown in Fig. 3(c). After these steps, we generate densely candidate grasp poses.

Then, a series of checks are performed to avoid invalid grasps.

Flatness detection. Let Ω denote the points on the contact area between the gripper and the object in T_p . Flatness detection first fits the plane equation P of the point set Ω , and then calculates the variance Var of Ω with mean as the plane equation:

$$Var = \sum_{i=0}^{n-1} \frac{\Omega_i - P}{n} \quad (14)$$

where n is the number of points in the set Ω . The grasps with variance greater than threshold are filtered out.

Force-closure metric. Force-closure metric [21] is met if the grasp axis lie within the friction cone at contact point, so that the object will not slide relative to the gripper. The friction cone is defined by the halfangle $\alpha = \arctan(\mu)$, where μ is the coefficient of friction [37]. μ is set to 0.2 to ensure that most objects can be grasped stably.

Collision detection. Collision detection is performed to prevent the gripper from colliding with objects.

After these steps we can generate densely distributed pixel-level grasp poses. All calculations are performed in synthetic depth images, which avoids covariate shift and improves calculation efficiency. We conduct simulation and real world grasp experiment in Sec. V-C and verify that the policy trained with grasps calculated in synthetic data performs well in the real world.

Compared to the labeling method of Dex-Net that the grasp labels for images from different viewpoints are all perpendicular to the table [4], the grasp labels for our images from different viewpoints are all parallel to the camera z-axis, which is shown in Fig. 6. When the table is full of clutter, the grasp network cannot extract the location feature of the table, so it cannot output grasp poses perpendicular to the table based on images from different viewpoints, which is contradictory to the grasp labels and reduces the performance. In contrast, our labels are only related to the camera position, so the network can output grasp poses parallel to the camera z-axis regardless

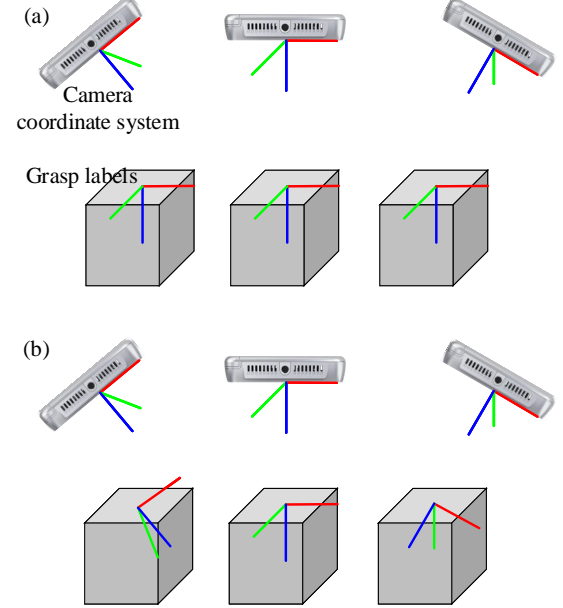


Fig. 6. The grasp labels for images from different viewpoints of (a) Dex-Net and (b) PLGP-Dataset. The grasp labels of Dex-Net are all perpendicular to the table, and our grasp labels are all parallel to the camera z-axis.

of whether the scene is simple or cluttered, which is consistent to the grasp labels.

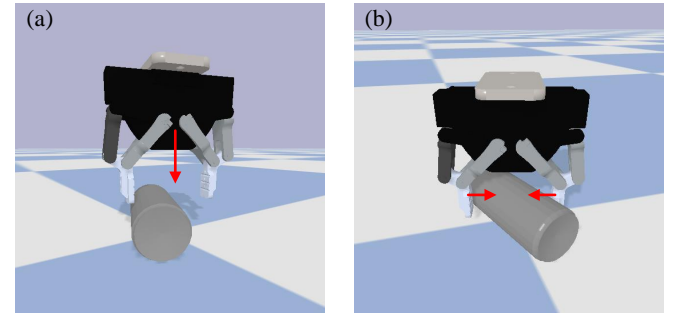


Fig. 7. (a) The grasp pose that causes the collision. (b) The grasp pose that does not achieve force-closure. As the gripper moves in the direction of the red arrow, the objects will be squeezed to a position suitable for grasping.

E. Evaluation

We design a bin picking benchmark for testing where 320 cluttered scenes are constructed using 77 seen objects and 77 novel objects. Seen objects refer to the objects used to construct the PLGP-Dataset. Both sets of objects are from model datasets including: 20 from ShapeNet [32], 8 from the YCB [33], and 49 from EGAD [34]. All objects are of different sizes, materials and shapes, and include food, utensils, tools, toys and other common life items. We further divide our test scenes into 4 categories according to the number of objects $m = \{5, 15\}$ and whether objects have been seen or novel.

To evaluate the performance, previous methods rely on the available information to calculate the grasp stability. The rectangle metric [10] considers a grasp as correct if the rotation error is less than 30° and the rectangle IOU is larger than

0.25, which do not take into account the impact of collisions or skidding. Fang *et al.* [6] believe that the correct grasp fits force-closure metric and collision detection. However, slight collisions and tilts sometimes do not cause the grasp to fail. The objects in Fig. 7 will be squeezed by the gripper to a position suitable for grasping.

In this work, we adopt intuitive simulation grasp to evaluate the grasp accuracy. For each predicted grasp pose and friction coefficient, a simulated gripper is driven to the grasp pose to close and then lift, the prediction is correct if the object is lifted to the specified location. For cluttered scene, grasp pose prediction algorithms are expected to predict multiple grasps. We compare performance on this benchmark with the following metrics:

- **Success Rate (SR):** Objects in the scenes are grasped one by one with the first-ranked grasp until either (a) no objects remain or (b) the robot has 5 consecutive failed grasps. Success Rate measures the percentage of grasp attempts that lift an object.
- **Percent Cleared (PC):** The fraction of objects that are lifted when the aforementioned grasp ends [5].
- **Average Precision (AP):** The average precision of top-50 ranked grasps. The scene is reset to its initial state after each grasp process.

We report all metrics as the average of the results at different μ ranging from 0.2 to 1.0, with $\Delta\mu = 0.2$ as interval. The simulation grasp processes for calculating SR, PC and AP are shown in Fig. 8.

Our benchmark renders RGB-D images and point clouds of the test scene in real-time after loading the object model according to the published poses. Other methods can read the required visual information to generate the grasp pose, and obtain the grasp results of the simulated gripper in real time for comparison.

IV. NETWORK

A. Network Architecture

Fully convolutional network (FCN) [38] is selected as the basic structure of our network since the grasp label is pixel-level. FCN is widely used for semantic segmentation of images [39–42]. Our previous work [25] prove that FCN is effective for predicting dense grasp poses. To verify that our dataset can effectively improve the performance of previous methods, we construct a pixel-level grasp detection network based on our previous network, AFFGA-Net [25]. AFFGA-Net first extracts features of different receptive fields and scales through the ResNet-101 network and the hybrid atrous spatial pyramid module, and then fuses the features according to different degrees of attention through an adaptive decoder, and finally outputs the grasping parameters through three task heads. Efficient feature extraction and decoding capabilities enable AFFGA-Net to perform best on the Cornell dataset [10].

We retain the encoder-decoder structure of AFFGA-Net as backbone and only modify the final task head to output grasp set $\tilde{G} = [Q_p, Q_\theta, W_g]$. \tilde{G} denotes the set of all grasps and corresponding qualities in the image space of size $H \times W$. We use Q_p to denote an output map of size $H \times W$ that represents

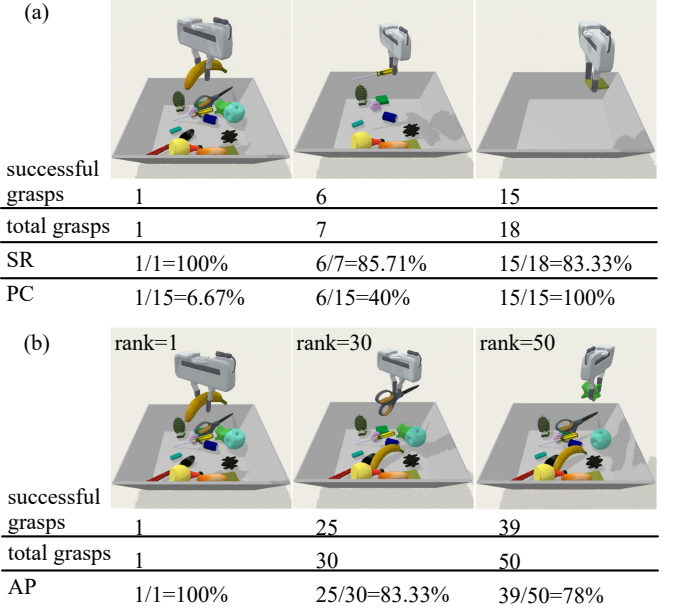


Fig. 8. The processes for calculating (a) Success Rate (SR), Percent Cleared (PC) and (b) Average Precision (AP). The scenes are initialized with 15 objects loaded. SR is the percentage of successful grasps out of total grasps. PC is the ratio of the successful grasps number to the objects number in the scene. AP is the percentage of successful grasps out of the top-50 grasps.

the quality of a grasp executed at each point p . Q_θ is an output map of size $K \times H \times W$, which is used to represent the quality of the grasp run at point p with angle category k , from which we calculate the grasp angle by $\theta = \frac{\pi}{K}k$. The values of Q_p and Q_θ are scalars in the range $[0, 1]$ where a value closer to 1 indicates higher quality. W_g is an output map of size $K \times H \times W$, which is used to represent the required gripper width w to execute a grasp at point p with angle $\theta = \frac{\pi}{K}k$. The value of W_g are in range of $[0, 1]$, and gripper width w is obtained by multiplying W_g by L_4 . Given the highest quality point p , highest quality angle θ and gripper width w , grasp depth d is calculated from the depth image so that the gripper does not collide with the scene, and d does not exceed L_3 . The network structure is shown in Fig. 9. The input to networks is an optional single RGB image, a depth image or a concatenate RGB-D image.

To test the effect of different backbones on the experimental results, we replace the backbone module with the previous grasp detection networks GGCNN2 [43], GRCNN [44] and semantic segmentation networks UNet [45], SegNet [46], DANet [47], DeepLabv3+ [48] and STDC [49]. The results are reported in Sec.V-B.

B. Enhancement and Normalization

We take all annotated grasp poses as positive samples and other grasp poses in the grasp parameter space as negative samples, and assume that all negative samples are unstable grasp poses. In PLGP-Dataset, the ratio of positive and negative samples is 1:1439. Significant imbalances in the number of samples degrade performance. In addition to using the focal loss function [50] to reduce the difference in loss of different samples, we also perform data enhancement on

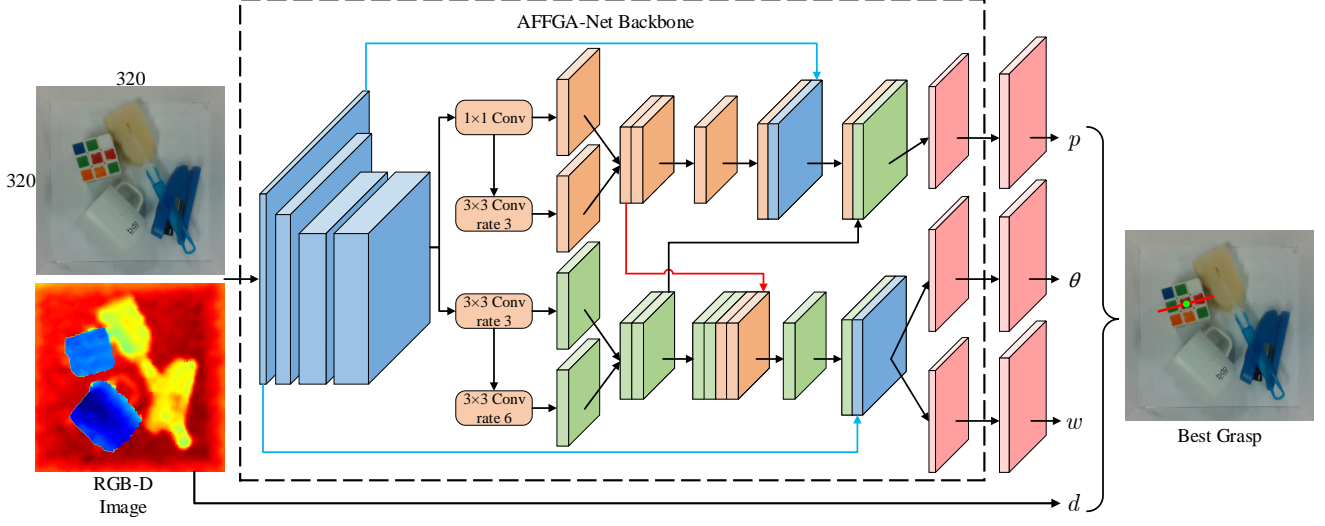


Fig. 9. Overview of our network. For a RGB-D image with $H \times W$ points as input, the network output the grasp quality, grasp angle quality and grasp width for every point. Given the highest quality point p , highest quality angle θ and gripper width w , grasp depth d is calculated from the depth image so that the gripper does not collide with the scene.

positive samples. Specifically, we copy the labeled grasp to other locations in its eight-neighborhood. The ratio is 1:317 after data enhancement. In Sec. V-A, we verify that data enhancement can effectively improve performance.

In order to facilitate the training of our network, we normalize the input depth image and learning target as follows.

Grasp quality. We treat grasp quality of each point as a scalar in the range $[0, 1]$. We set the already labeled grasp points a value of 1, and set the enhanced points a value of 0.9. All other points are 0.

Grasp angle. Each grasp angle θ is labeled in the range $[0, \pi]$. We convert the angle θ into category $k = \lfloor \frac{\theta}{\pi} K \rfloor$, where $K = 18$. We treat the quality of the grasps run at point p with angle category k as a scalar in the range $[0, 1]$. The already labeled grasp angles are set to 1, and the enhanced grasp angles are set to 0.9. All other angles are 0.

Gripper width. We scale the values of w by $\frac{1}{L_4}$ to put it in the range $[0, 1]$.

Input images. To augment the dataset, we perform data enhancement on images. We take a centre crop of 320×320 pixels with random translation up to 30 pixels horizontally and vertically. This image patch is then randomly rotated up to 30 degrees in both clock-direction and anticlock-direction. Then the image is randomly flipped horizontally. Finally, we subtract the mean of each image, centering its value around 0 to provide invariance.

C. Loss Function

Since the values of the network output map are all in the range of $[0, 1]$, the sigmoid function is used to activate the output value. GGCNN2 [43] uses the mean square error function to calculate the loss. However, the update rate is very slow when the prediction is close to the ground truth. We use the binary focal loss function to calculate the loss to avoid gradient reduction and reduce the loss difference between

positive and negative samples. The loss function is defined as:

$$L(P, P^*, H, W, K) = -\frac{1}{N} \sum_{i=0}^H \sum_{j=0}^W \sum_{k=0}^K ((P_{ijk}^* \cdot \log(P_{ijk})) + (1 - P_{ijk}^*) \cdot \log(1 - P_{ijk})) \cdot |P_{ijk} - P_{ijk}^*|^\gamma \cdot \alpha, \quad (15)$$

where P is the output map of size $K \times H \times W$, P^* is training target, γ is set to 2 as recommended by [50]. Our network has the highest success rate in test scenarios when α is set to 0.95.

During training, the whole network is updated by minimizing the follow objective function:

$$L_{total} = \beta_1 \cdot L(Q_p, Q_p^*, H, W, 1) + \beta_2 \cdot L(Q_\theta, Q_\theta^*, H, W, K) + \beta_3 \cdot L(W_g, W_g^*, H, W, K) \quad (16)$$

where β_1 , β_2 and β_3 are weight coefficients of the loss. In our study, we experimentally set $\beta_1 = 10$, $\beta_2 = 10$ and $\beta_3 = 20$.

V. EXPERIMENTS

In this section, we first conduct ablation studies to show the effectiveness of loss function and data enhancement. Then, we benchmark several backbone networks and representative methods on our test scenes and compare them with our method in unified evaluation metrics. Finally, we conduct robotic experiments in real-world to demonstrate that our method can overcome the gap between simulation and reality.

A. Ablation Studies

All networks are implemented with PyTorch and trained with Adam optimizer [51] on a PC running Ubuntu 16.04 with a 3.5GHz Intel Core i9-9900 CPU and NVIDIA TITAN-XP graphics card. The initial learning rate is set to 0.001.

TABLE II
EVALUATION FOR NETWORKS WITH DIFFERENT BACKBONE ON BENCHMARK.

Backbone	Input	Seen (%)						Novel (%)						Params (M)	GFLOPs
		5 objects			15 objects			5 objects			15 objects				
		SR	PC	AP	SR	PC	AP	SR	PC	AP	SR	PC	AP		
GGCNN2	Depth	70.49	94.47	77.87	59.96	72.47	66.99	68.40	90.06	86.15	62.59	81.63	75.18	0.079	1.36
	RGB	59.88	82.54	77.97	47.80	47.46	57.65	27.46	43.02	28.43	27.00	20.48	7.49	0.083	1.56
	RGB-D	65.34	89.80	75.68	50.85	57.54	62.86	29.26	52.80	30.33	32.16	30.20	6.47	0.085	1.66
GRCNN	Depth	73.44	95.74	82.92	60.87	77.18	72.05	75.49	93.13	89.47	68.05	84.63	82.70	1.90	13.38
	RGB	60.17	83.67	72.76	48.84	51.32	55.46	27.85	46.38	28.25	30.68	25.66	6.36	1.90	13.64
	RGB-D	64.43	88.01	77.61	51.27	58.76	59.25	30.47	55.71	29.84	33.97	35.30	7.23	1.91	13.77
UNet	Depth	73.74	93.92	83.89	61.74	72.58	76.98	76.95	93.43	88.39	67.20	84.20	79.90	34.53	50.18
	RGB	67.65	89.82	74.96	50.44	51.25	55.14	63.14	82.33	81.74	55.51	57.98	66.92	34.53	50.24
	RGB-D	63.75	86.17	75.67	52.20	55.47	60.90	61.91	88.19	82.98	56.48	65.35	68.30	34.53	50.27
SegNet	Depth	73.94	95.03	84.89	62.18	76.25	73.13	76.34	93.33	89.05	67.19	84.66	79.12	29.54	35.41
	RGB	66.66	91.17	76.74	51.42	56.04	64.42	65.21	85.55	83.05	57.22	64.34	67.41	29.54	35.46
	RGB-D	64.58	89.33	80.40	54.01	64.52	66.46	62.34	88.24	84.57	59.08	73.91	71.52	29.54	35.49
DeepLabv3+	Depth	55.30	79.29	73.23	50.52	55.15	71.12	66.17	87.65	83.54	62.21	77.75	78.14	62.02	83.45
	RGB	54.26	77.47	66.69	45.62	43.95	58.94	59.96	83.27	79.75	55.18	60.44	71.41	62.02	83.53
	RGB-D	56.20	80.27	69.20	47.02	48.64	64.63	58.81	84.93	82.17	52.77	60.88	66.55	62.03	83.57
STDC	Depth	74.49	96.17	82.43	62.10	73.74	71.60	75.02	93.18	90.68	68.00	85.49	82.66	47.58	39.25
	RGB	67.18	92.03	80.41	50.92	53.51	60.80	65.66	83.37	82.02	57.13	63.42	71.87	47.58	39.26
	RGB-D	61.62	82.32	77.08	52.97	59.83	61.96	63.71	86.68	86.10	57.28	69.15	73.10	47.58	39.27
DANet	Depth	81.31	96.22	87.79	69.43	86.55	76.59	80.11	94.28	89.59	69.25	85.64	78.14	26.18	25.33
	RGB	69.87	92.84	82.86	55.78	64.15	66.14	66.74	87.67	83.16	60.67	69.16	68.64	26.19	25.36
	RGB-D	79.29	96.60	87.97	68.37	79.83	76.73	74.42	91.40	89.97	67.24	79.49	77.06	26.19	25.37
AFFGA-Net (Ours)	Depth	83.14	96.39	84.67	75.30	85.84	75.25	80.41	92.02	91.13	65.61	84.79	87.37	67.59	29.58
	RGB	74.40	86.71	77.66	71.02	75.65	74.65	82.92	94.07	90.68	63.24	67.42	75.71	67.60	29.67
	RGB-D	85.59	96.20	89.47	78.81	85.78	78.33	84.48	96.80	94.07	70.86	84.87	85.49	67.60	29.70

TABLE III
ABLATION STUDIES.

Baseline	Enhance	BFL	SR (%)	PC (%)	AP (%)
✓			25.28	17.87	38.91
✓	✓		60.45	78.13	82.44
✓		✓	67.30	84.85	81.75
✓	✓	✓	70.86	84.87	85.49

* **BFL:** Binary focal loss function.

Networks are trained end-to-end for 100 epochs and learning rate decays by a factor of 0.1 at 70 epochs.

In order to verify the effectiveness of binary focal loss function and data enhancement, we conduct ablation studies on the test scenes containing 15 novel objects, and the network input is a depth image. We follow the steps below to improve the AFFGA-Net and test its performance. (1) Modify the final task head to output grasp set \tilde{G} . (2) Perform data enhancement on labeled grasps. (3) Use the binary focal loss function instead of the binary cross-entropy function to calculate the loss. (4) Combination of (2) and (3).

Results are reported in Table III. Baseline achieves only 25.28%, 17.87% and 38.91% on the SR, PC and AP, respectively. Data enhancement improves accuracies by 35.17%, 60.26% and 43.53%, and binary focal loss function improves

accuracies by 42.02%, 66.98% and 42.84% compared to the baseline, respectively. The great improvement is due to data augmentation and binary focal loss significantly alleviating the imbalance of positive and negative samples. Combining data enhancement and binary focal loss function gives the highest accuracies.

B. Performance on Benchmark

We first test the effect of different backbone networks on the experimental results in the benchmark. Then we test different representative methods on our benchmark and compare them with our method.

For depth image based method, we adopt GQCNN [3] and FC-GQCNN [9]. For point cloud based method, we adopt GraspNet [6]. GQCNN first samples multiple candidate grasp poses based on the depth image, and then input the image patch centered on the grasp point together with the point cloud into the grasp quality classification network to obtain the quality of each candidate grasp pose. FC-GQCNN outputs multiple 4-DOF grasp poses and qualities on depth images end-to-end. GraspNet takes point cloud as input and predicts approaching direction, grasp pose and quality through three network modules connected in series. Since the output data formats are different, we adopt the public weights of GQCNN, FC-GQCNN and GraspNet which are trained on Dex-net

4.0 [3], Dex-net 2.0 [4] and GraspNet-1Billion [6] datasets, respectively.

The experimental results of networks built on different backbones when inputting depth images, RGB images, and RGB-D images are shown in Table II.

Comparing the results of the same network with different input, the network with depth image as input has better performance than RGB image, because the depth image contains the shape information of the objects. The difference in accuracy is especially noticeable in lightweight networks, because it is difficult for lightweight networks to extract shape features related to grasping from color information. For example, the differences between SR, PC and AP of GGCNN2 with RGB images and depth images as input in scenes containing 5 novel objects are 40.94%, 47.04% and 57.72%, respectively, while the differences of UNet are 13.81%, 11.10% and 6.65%. In addition, the results of complex networks with RGB-D images and depth images as input is similar, while the accuracy of lightweight networks with RGB-D images as input is lower, which is due to the inability of lightweight networks to fit complex data distributions.

Compared with complex networks or lightweight networks with depth images as input, lightweight networks with RGB and RGB-D images as input have a larger accuracy gap between seen objects and novel objects, and the gap in AP is more obvious in the scene containing 15 objects. This indicates that lightweight networks with RGB image as input are more prone to overfitting, and the actual quality of predicted grasp pose drops drastically as the predicted quality decreases.

Comparing the results of the same network in scenes with different levels of complexity, all networks perform better in scenes containing 5 objects, because complex scenes have low error tolerance for grasp poses, slight grasp point errors and collisions can cause objects to move and fail to grasp. Besides, networks taking depth images as input are less affected by scene complexity than networks taking RGB images as input, because color information cannot reflect the positional relationship of stacked objects. For example, the differences between SR, PC and AP of STDC with depth images as input in scenes containing 15 and 5 seen objects are 7.02%, 7.69% and 8.02%, respectively, while the differences of STDC with RGB images as input are 8.53%, 19.95% and 10.15%.

Comparing the results of different networks under the same input, our AFFGA-Net performs best. The reason contribute to this achievement is, the hybrid atrous spatial pyramid module extracts features of different receptive fields and scales, and the adaptive decoder provides the most relevant features for different prediction tasks. DeepLabv3+, which is popular in the semantic segmentation, is inferior to UNet in the grasp detection task. This is because DeepLabv3+ directly enlarges the feature map by upsampling to obtain the prediction map by 4 times, and cannot accurately recover the pixel-level grasping pose.

We separately test the performance of GQCNN, FC-GQCNN and GraspNet in benchmark scenes containing novel objects, and compare with our network. The SR, PC and AP of the methods under different friction coefficients are shown in Fig. 10, and the mean values of SR, PC and AP under different

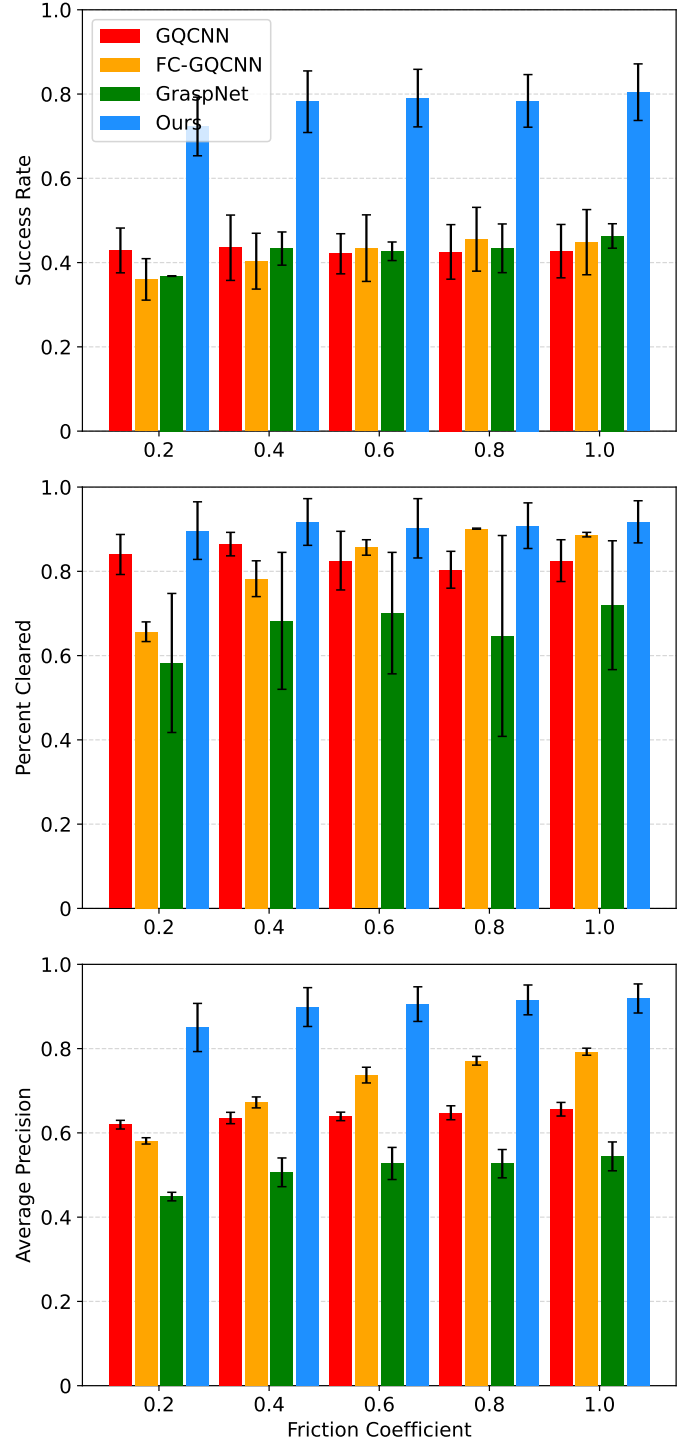


Fig. 10. The SR, PC and AP of different methods under different friction coefficients. The value and error of each bar are the mean and difference of the method's metrics in scenes with 5 and 15 objects, respectively.

TABLE IV
EVALUATION FOR DIFFERENT METHODS ON BENCHMARK.

Method	Input	5 objects			15 objects		
		SR (%)	PC (%)	AP (%)	SR (%)	PC (%)	AP (%)
GQCNN [3]	Depth	36.62	87.95	65.29	48.88	78.42	62.62
FC-GQCNN [9]	Depth	35.08	83.45	69.92	48.98	79.92	72.24
GraspNet [6]	Point cloud	45.48	83.90	54.08	39.53	49.38	48.07
AFFGA-Net (Ours)	RGB-D	84.48	96.80	94.07	70.86	84.87	85.49

friction coefficients are shown in Table IV. The results show that our method outperforms other methods at all friction coefficients and metrics.

Compared with GQCNN, even the light-weight network GGCNN with depth images as input improves the SR, PC and AP metrics of scenes containing 5 unknown objects by 31.78%, 2.11% and 20.86%, respectively. This is because the candidate grasping poses randomly generated by GQCNN cannot be guaranteed to be globally optimal and cannot cover the grasp parameter space. In addition, the Dex-Net and GraspNet-1Billion datasets generate grasp pose labels based on 3D object models and then use point clouds or depth images to train networks, which makes the data distribution of network training and testing different, thereby reducing the generalization ability of GQCNN, FC-GQCNN and GraspNet. This further shows that datasets with on-policy and pixel-level attributes can effectively improve grasp detection performance.

All networks constructed in this paper are only different from the original networks in the head part, and there is no targeted improvement for grasp detection tasks, which means that the network structure and grasping accuracy can still be improved.

C. Real-world Grasping

To perform robotic grasping experiments, we use a Kinova Gen2 7DOF robot fitted with a robotiq 2f-140 gripper. Our camera is an Intel RealSense D435i RGB-D camera and is mounted to the wrist of the robot. We selected 40 objects of different shapes, sizes, and materials for testing. This set-up is shown in Fig. 11.

We conduct three sets of experiments to separately test the performance of AFFGA-Net in scenes containing $M = \{1, 5, 10\}$ objects. Objects are randomly ordered and numbered before the experiment began. In the initial state of each scene, we select M objects in number order and place them randomly in the tray. On each timestep, with the AFFGA-Net, we input a RGB-D image and camera intrinsics, and output the 6-DOF grasp pose with highest predicted quality. The robot then approaches the target and closes the jaws (Fig. 12). Grasp success is defined by whether or not the grasp transport the target object to the receptacle. If there are no objects in the tray or the robot has 5 consecutive failures, the next scene will be tested. Each object is placed in the tray a total of 10 times.

Table V shows the performance. We conduct a total of 2,428 grasping trials, and the total number of failed grasps is 28. Grasping success rate decreases as the test scenes contains



Fig. 11. Left: Set-up for robotic grasping experiments. For each experiment, M objects are randomly dropped on the tray, at which point the robot iteratively plans grasps from RGB-D image and attempts to lift and transport the objects to a receptacle. Right: A set of 40 test objects.

TABLE V
ROBOTIC GRASP RESULTS.

Objects	SR (%)	PC (%)	Attempts	Failures
1	99.01	100	404	4
5	98.28	100	407	7
10	95.92	100	417	17

more objects, because stacked objects increase the error of the depth images and squeeze the positive grasping parameter space. However, the success rate in the scenes consisting of 10 objects still reaches 95.92%. Meanwhile, the percent cleared are 100% in all experiments. There are three main types of failed grasping: (1) Adjacent objects are grasped at the same time, and drop during lift; (2) Large cylindrical objects cannot be grasped when placed vertically; (3) Objects with sloping edges cannot be grasped. The first kind of failure is due to the inability of the network to distinguish two objects that are in close proximity. The second kind of failure is due to fewer training scenes with upright cylindrical objects in the PLGP-Dataset. The third kind of failure is due to the low friction coefficient threshold (i.e. 0.2) for filtering out candidate grasp poses in the PDG-Generation method, resulting in fewer grasp

successes.

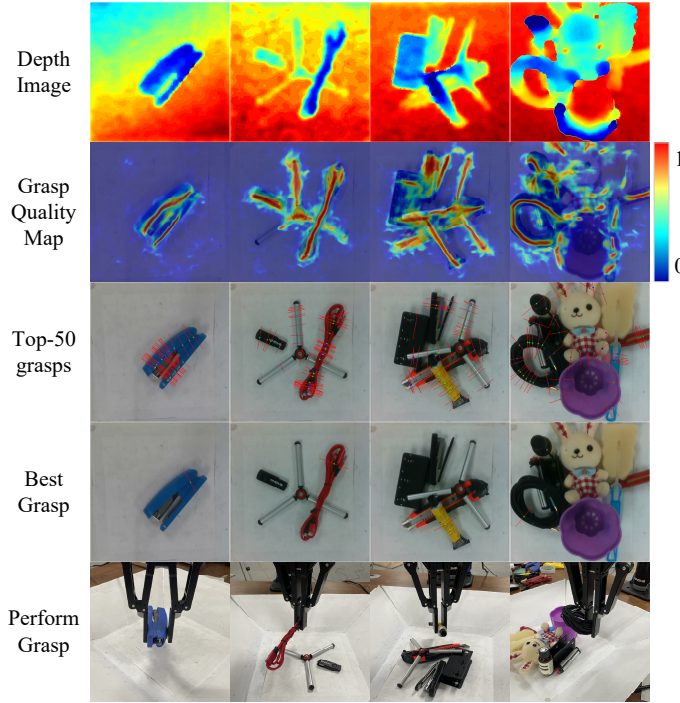


Fig. 12. Experiments for real-world robotic grasping.

pose labels on objects with sloping edges. The experimental procedure is shown in the supplemental video¹.

VI. CONCLUSION

In this paper, we propose an on-policy grasp detection method. First, the PDG-Generation method is introduced to compute pixel-level grasp labels based on parallel depth images, which trains and tests the grasping network on the same distribution, and improves the generalization ability of the network. Then, the first on-policy pixel-level grasp detection dataset PLGP-Dataset is constructed and released based on PDG-Generation method. It consists of images taken by the simulated sensor, with rich and dense annotations. At last, we construct a series of grasp detection networks equipped with a novel data augmentation mode. Extensive experiments demonstrate the superiority of our method in both bin-picking benchmark and real grasping. Our future work is to expand the dataset and drive the robot to push objects autonomously to improve grasping success rate.

ACKNOWLEDGMENT

This work is supported in part by National Natural Science Foundation of China (62176138, 62176136), National Key R&D Program of China (NO.2018YFB1305300), Shandong Provincial Key Research and Development Program (Major Scientific and Technological Innovation Project) (NO.2019JZZY010130, 2020CXGC010207).

REFERENCES

- [1] N. D. Kahanowich and A. Sintov, “Robust classification of grasped objects in intuitive human-robot collaboration using a wearable force-myography device,” *IEEE Robotics and Automation Letters*, vol. 6, no. 2, pp. 1192–1199, 2021.
- [2] F. Y. Wu and H. H. Asada, “Implicit and intuitive grasp posture control for wearable robotic fingers: a data-driven method using partial least squares,” *IEEE Transactions on Robotics*, vol. 32, no. 1, pp. 176–186, 2016.
- [3] J. Mahler, M. Matl, V. Satish, M. Danielczuk, B. DeRose, S. McKinley, and K. Goldberg, “Learning ambidextrous robot grasping policies,” *Science Robotics*, vol. 4, no. 26, 2019.
- [4] J. Mahler, J. Liang, S. Niyaz, M. Laskey, R. Doan, X. Liu, J. A. Ojea, and K. Goldberg, “Dex-net 2.0: Deep learning to plan robust grasps with synthetic point clouds and analytic grasp metrics,” in *Robotics: Science and Systems*, 2017.
- [5] M. Jeffrey and G. Ken, “Learning deep policies for robot bin picking by simulating robust grasping sequences,” in *Conference on robot learning*, pp. 515–524, 2017.
- [6] H.-S. Fang, C. Wang, M. Gou, and C. Lu, “Graspnet-1billion: A large-scale benchmark for general object grasping,” in *Proceedings of the IEEE/CVF conference on computer vision and pattern recognition*, pp. 11444–11453, 2020.
- [7] Z. Binglei, Z. Hanbo, L. Xuguang, W. Haoyu, T. Zhiqiang, and Z. Nanning, “Regnet: Region-based grasp network for end-to-end grasp detection in point clouds,” in *2021 IEEE International Conference on Robotics and Automation (ICRA)*, pp. 13474–13480, 2021.
- [8] L. Pinto and A. Gupta, “Supersizing self-supervision: Learning to grasp from 50k tries and 700 robot hours,” in *2016 IEEE international conference on robotics and automation (ICRA)*, pp. 3406–3413, 2016.
- [9] V. Satish, J. Mahler, and K. Goldberg, “On-policy dataset synthesis for learning robot grasping policies using fully convolutional deep networks,” *IEEE Robotics and Automation Letters*, vol. 4, no. 2, pp. 1357–1364, 2019.
- [10] Y. Jiang, S. Moseson, and A. Saxena, “Efficient grasping from rgbd images: Learning using a new rectangle representation,” in *2011 IEEE International conference on robotics and automation*, pp. 3304–3311, 2011.
- [11] A. Depierre, E. Dellandréa, and L. Chen, “Jacquard: A large scale dataset for robotic grasp detection,” in *2018 IEEE/RSJ International Conference on Intelligent Robots and Systems (IROS)*, pp. 3511–3516, 2018.
- [12] E. Coumans and Y. Bai, “Pybullet, a python module for physics simulation for games, robotics and machine learning,” <http://pybullet.org>, 2016–2021.
- [13] S. Levine, P. Pastor, A. Krizhevsky, J. Ibarz, and D. Quillen, “Learning hand-eye coordination for robotic grasping with deep learning and large-scale data collection,” *The International Journal of Robotics Research*, vol. 37, no. 4-5, pp. 421–436, 2018.

¹https://youtu.be/XFUb1_oZ9WQ

[14] H. Zhang, X. Lan, S. Bai, X. Zhou, Z. Tian, and N. Zheng, “Roi-based robotic grasp detection for object overlapping scenes,” in *2019 IEEE/RSJ International Conference on Intelligent Robots and Systems (IROS)*, pp. 4768–4775, 2019.

[15] F.-J. Chu, R. Xu, and P. A. Vela, “Real-world multiobject, multigrasp detection,” *IEEE Robotics and Automation Letters*, vol. 3, no. 4, pp. 3355–3362, 2018.

[16] X. Yan, J. Hsu, M. Khansari, Y. Bai, A. Pathak, A. Gupta, J. Davidson, and H. Lee, “Learning 6-dof grasping interaction via deep geometry-aware 3d representations,” in *2018 IEEE International Conference on Robotics and Automation (ICRA)*, pp. 3766–3773, 2018.

[17] J. Bohg, A. Morales, T. Asfour, and D. Kragic, “Data-driven grasp synthesis-a survey,” *IEEE Transactions on Robotics*, vol. 30, no. 2, pp. 289–309, 2013.

[18] Y. Inagaki, R. Araki, T. Yamashita, and H. Fujiyoshi, “Detecting layered structures of partially occluded objects for bin picking,” in *2019 IEEE/RSJ International Conference on Intelligent Robots and Systems (IROS)*, pp. 5786–5791, 2019.

[19] B. Wu, I. Akinola, A. Gupta, F. Xu, J. Varley, D. Watkins-Valls, and P. K. Allen, “Generative attention learning: a “general” framework for high-performance multi-fingered grasping in clutter,” *Auton. Robots*, vol. 44, no. 6, pp. 971–990, 2020.

[20] S. R. Lakani, A. J. Rodríguez-Sánchez, and J. H. Piater, “Towards affordance detection for robot manipulation using affordance for parts and parts for affordance,” *Auton. Robots*, vol. 43, no. 5, pp. 1155–1172, 2019.

[21] V.-D. Nguyen, “Constructing force-closure grasps,” *The International Journal of Robotics Research*, vol. 7, no. 3, pp. 3–16, 1988.

[22] Q. Yu, W. Shang, Z. Zhao, S. Cong, and Z. Li, “Robotic grasping of unknown objects using novel multilevel convolutional neural networks: From parallel gripper to dexterous hand,” *IEEE Transactions on Automation Science and Engineering*, 2020.

[23] I. Akinola, A. Angelova, Y. Lu, Y. Chebotar, D. Kalashnikov, J. Varley, J. Ibarz, and M. S. Ryoo, “Visionary: Vision architecture discovery for robot learning,” pp. 10 779–10 785, 2021.

[24] S. Ainetter and F. Fraundorfer, “End-to-end trainable deep neural network for robotic grasp detection and semantic segmentation from rgb,” in *2021 IEEE International Conference on Robotics and Automation (ICRA)*, pp. 13 452–13 458, 2021.

[25] D. Wang, C. Liu, F. Chang, N. Li, and G. Li, “High-performance pixel-level grasp detection based on adaptive grasping and grasp-aware network,” *IEEE Transactions on Industrial Electronics*, 2021.

[26] F.-J. Chu, R. Xu, and P. A. Vela, “Real-world multi-object, multi-grasp detection,” *IEEE Robotics and Automation Letters*, vol. 3, no. 4, pp. 3355–3362, 2018.

[27] F. Alladkani, J. Akl, and B. Calli, “Ecnns: Ensemble learning methods for improving planar grasp quality estimation,” pp. 4769–4775, 2021.

[28] X. Zhu, L. Sun, Y. Fan, and M. Tomizuka, “6-dof contrastive grasp proposal network,” pp. 6371–6377, 2021.

[29] L. Berscheid, C. Friedrich, and T. Kröger, “Robot learning of 6 dof grasping using model-based adaptive primitives,” pp. 4474–4480, 2021.

[30] K. S. Andreas ten Pas, Marcus Gualtieri and R. P. Jr., “Grasp pose detection in point clouds,” *Int. J. Robotics Res.*, vol. 36, no. 13-14, pp. 1455–1473, 2017.

[31] Y. Qin, R. Chen, H. Zhu, M. Song, J. Xu, and H. Su, “S4g: Amodal single-view single-shot $se(3)$ grasp detection in cluttered scenes,” in *Conference on robot learning*, pp. 53–65, 2020.

[32] A. X. Chang, T. Funkhouser, L. Guibas, P. Hanrahan, Q. Huang, Z. Li, S. Savarese, M. Savva, S. Song, H. Su *et al.*, “Shapenet: An information-rich 3d model repository,” *arXiv preprint arXiv:1512.03012*, 2015.

[33] B. Calli, A. Walsman, A. Singh, S. Srinivasa, P. Abbeel, and A. M. Dollar, “Benchmarking in manipulation research: Using the yale-cmu-berkeley object and model set,” *IEEE Robotics & Automation Magazine*, vol. 22, no. 3, pp. 36–52, 2015.

[34] D. Morrison, P. Corke, and J. Leitner, “Egad! an evolved grasping analysis dataset for diversity and reproducibility in robotic manipulation,” *IEEE Robotics and Automation Letters*, vol. 5, no. 3, pp. 4368–4375, 2020.

[35] E. Johns, S. Leutenegger, and A. J. Davison, “Deep learning a grasp function for grasping under gripper pose uncertainty,” in *2016 IEEE/RSJ International Conference on Intelligent Robots and Systems (IROS)*, pp. 4461–4468. IEEE, 2016.

[36] S. Zennaro, M. Munaro, S. Milani, P. Zanuttigh, A. Bernardi, S. Ghidoni, and E. Menegatti, “Performance evaluation of the 1st and 2nd generation kinect for multimedia applications,” in *2015 IEEE International Conference on Multimedia and Expo (ICME)*, pp. 1–6. IEEE, 2015.

[37] G. Smith, E. Lee, K. Goldberg, K. Bohringer, and J. Craig, “Computing parallel-jaw grips,” in *Proceedings 1999 IEEE International Conference on Robotics and Automation (Cat. No. 99CH36288C)*, vol. 3, pp. 1897–1903, 1999.

[38] J. Long, E. Shelhamer, and T. Darrell, “Fully convolutional networks for semantic segmentation,” in *Proceedings of the IEEE conference on computer vision and pattern recognition*, pp. 3431–3440, 2015.

[39] T. Zhou, W. Wang, S. Liu, Y. Yang, and L. Van Gool, “Differentiable multi-granularity human representation learning for instance-aware human semantic parsing,” in *Proceedings of the IEEE/CVF Conference on Computer Vision and Pattern Recognition*, pp. 1622–1631, 2021.

[40] L. Zhu, D. Ji, S. Zhu, W. Gan, W. Wu, and J. Yan, “Learning statistical texture for semantic segmentation,” in *Proceedings of the IEEE/CVF Conference on Computer Vision and Pattern Recognition*, pp. 12 537–12 546, 2021.

[41] T. Takikawa, D. Acuna, V. Jampani, and S. Fidler, “Gated-scnn: Gated shape cnns for semantic segmentation,” in *Proceedings of the IEEE/CVF International Conference on Computer Vision*, pp. 5229–5238, 2019.

- [42] Y. Yuan, J. Xie, X. Chen, and J. Wang, “Segfix: Model-agnostic boundary refinement for segmentation,” in *European Conference on Computer Vision*, pp. 489–506, 2020.
- [43] D. Morrison, P. Corke, and J. Leitner, “Learning robust, real-time, reactive robotic grasping,” *The International Journal of Robotics Research*, vol. 39, no. 2-3, pp. 183–201, 2020.
- [44] S. Kumra, S. Joshi, and F. Sahin, “Antipodal robotic grasping using generative residual convolutional neural network,” in *2020 IEEE/RSJ International Conference on Intelligent Robots and Systems (IROS)*, pp. 9626–9633, 2020.
- [45] O. Ronneberger, P. Fischer, and T. Brox, “U-net: Convolutional networks for biomedical image segmentation,” in *International Conference on Medical image computing and computer-assisted intervention*, pp. 234–241, 2015.
- [46] V. Badrinarayanan, A. Kendall, and R. Cipolla, “Segnet: A deep convolutional encoder-decoder architecture for image segmentation,” *IEEE transactions on pattern analysis and machine intelligence*, vol. 39, no. 12, pp. 2481–2495, 2017.
- [47] J. Fu, J. Liu, H. Tian, Y. Li, Y. Bao, Z. Fang, and H. Lu, “Dual attention network for scene segmentation,” in *Proceedings of the IEEE/CVF Conference on Computer Vision and Pattern Recognition*, pp. 3146–3154, 2019.
- [48] L.-C. Chen, Y. Zhu, G. Papandreou, F. Schroff, and H. Adam, “Encoder-decoder with atrous separable convolution for semantic image segmentation,” in *Proceedings of the European conference on computer vision (ECCV)*, pp. 801–818, 2018.
- [49] M. Fan, S. Lai, J. Huang, X. Wei, Z. Chai, J. Luo, and X. Wei, “Rethinking bisenet for real-time semantic segmentation,” in *Proceedings of the IEEE/CVF Conference on Computer Vision and Pattern Recognition*, pp. 9716–9725, 2021.
- [50] T.-Y. Lin, P. Goyal, R. Girshick, K. He, and P. Dollár, “Focal loss for dense object detection,” in *Proceedings of the IEEE international conference on computer vision*, pp. 2980–2988, 2017.
- [51] D. P. Kingma and J. Ba, “Adam: A method for stochastic optimization,” *arXiv preprint arXiv:1412.6980*, 2014.